

Uncertainty Modeling and Experiments in \mathcal{H}_∞ Control of Large Flexible Space Structures

Benoit Boulet, *Member, IEEE*, Bruce A. Francis, *Fellow, IEEE*, Peter C. Hughes, and Tony Hong

Abstract—Approaches to uncertainty modeling for robust control of large flexible space structures (LFSS's) such as additive or multiplicative perturbations in \mathcal{H}_∞ do not work very well because of the special properties of LFSS dynamics. In this paper, we propose the use of a left-coprime factorization (LCF) of LFSS dynamics in modal coordinates in order to get improved stability margins and performance in robust control design. The plant uncertainty is then described as stable perturbations of the coprime factors accounting for modal parameter uncertainty and unmodeled dynamics. Two multivariable \mathcal{H}_∞ designs based on LCF's of 46th-order collocated and noncollocated models of an LFSS experimental testbed are presented together with simulation and experimental results to illustrate the technique.

Index Terms—Coprime factorization, digital control, flexible structures, robustness, space vehicle control, uncertain systems, \mathcal{H} -infinity control, vibration control.

I. INTRODUCTION

THE dynamics of large flexible space structures (LFSS's) are characterized by their high order and their significant number of closely spaced, lightly damped, clustered low-frequency modes. Mathematical linear dynamic models of LFSS are usually obtained using finite-element (FE) methods, but these models are known to be accurate only for the first few modes of the structure. Thus, uncertainty modeling in LFSS is critical if one is to achieve an acceptable level of robustness with a practical controller.

Some works [1], [17] use norm-bounded additive or multiplicative perturbations of a nominal model in the frequency domain to account for uncertainty in the modal frequencies, damping ratios, and mode shape matrix of the model. Unmodeled modes of the structure and uncertain actuator dynamics can also be represented in this way [13]. Such approaches to uncertainty modeling in LFSS do not handle modal parameter uncertainty very well: Slight variations in either the modal frequencies or damping ratios usually cause the associated dynamic perturbations to be large in the ∞ -norm sense.

Manuscript received July 25, 1995; revised September 1, 1996 and April 7, 1997. Recommended by Associate Editor, F. Hadaegh. B. Boulet was supported by scholarships from the Natural Sciences and Engineering Research Council (NSERC) of Canada, the Fonds pour la formation de chercheurs et l'aide à la recherche, Québec, and a W. C. Sumner Memorial Fellowship. B. A. Francis and P. C. Hughes were supported by NSERC.

B. Boulet is with Hatch Associates Ltd., Mississauga, Ontario, Canada L5K 2R7.

B. A. Francis is with the Systems Control Group, Department of Electrical and Computer Engineering, University of Toronto, Toronto, Ontario, Canada M5S 1A4.

P. C. Hughes and T. Hong are with the Institute for Aerospace Studies, University of Toronto, North York, Ontario, Canada M3H 5T6.

Publisher Item Identifier S 1063-6536(97)06203-9.

Covering unmodeled modes with such perturbations suffers from the same problem, leading to low-performance control system designs. In [17], an eigenvalue perturbation approach to modeling uncertainty in the low-frequency modes was also tested experimentally and showed good performance, although the uncertainty regions covered only 1% error in damping ratios and 0.1% error in modal frequencies.

In this paper, it is suggested to transform real parameter uncertainty in the modes into unstructured uncertainty, without getting too conservative in the sense that the uncertainty set in \mathcal{H}_∞ has to be kept relatively small. The unstructured uncertainty model allows the use of reliable \mathcal{H}_∞ controller design algorithms (available, e.g., in Matlab) that work for high-dimensional systems.

A more direct approach would be to model the uncertainty as real bounded perturbations, which leads to the mixed real/complex μ problem. This problem has been studied recently [9] and design methods based on minimizing an upper bound on the mixed μ function, such as the so-called Popov controller synthesis, have been developed. An application to a flexible structure has been reported in [11]. These methods are attractive, but they quickly become numerically difficult (actually, they are NP-hard) as the plant's order and the number of independent perturbations increase.

Some authors have argued (e.g., [18]) that coprime factorizations (CF's) in \mathcal{H}_∞ of nearly unstable plants, such as LFSS, is a sound way to model these systems. This is the approach taken here, as introduced in [3]. The similar design techniques of loopshaping [14] and weighted-gap optimization [5] applied to LFSS both use a normalized CF of LFSS dynamics. The good results obtained in [5] and [14] with these techniques show the potential of modeling LFSS dynamics using coprime factorizations, but they do not address the problem of converting known uncertainty bounds on the modal parameters into norm bounds on factor perturbations. The difficulty comes from the fact that these methods rely on *normalized* coprime factorizations, which destroy the decoupled structure of the nominal modal state-space models.

Section II presents a simple method to obtain a left-coprime factorization (LCF) of LFSS dynamics in modal coordinates that preserves the decoupled structure. Uncertainty modeling is discussed in Section III. In Section IV, two multivariable \mathcal{H}_∞ designs based on LCF's of two 46th-order collocated and noncollocated models of an LFSS experimental testbed called Daisy are presented together with some simulation and experimental results.

Notation. The norm of a complex matrix is taken to be its maximum singular value: $\|H\| = \bar{\sigma}(H)$. The transpose of H is denoted as H^T . For x in \mathbb{R}^n , $\|x\|_\infty = \max_{i=1, \dots, n} |x_i|$. We denote the open and closed right-half complex planes by \mathbb{C}_+ and $\bar{\mathbb{C}}_+$, respectively. The space \mathcal{H}_∞ is the class of functions analytic in \mathbb{C}_+ and bounded on the imaginary axis with norm defined as $\|Q\|_\infty = \sup_{\omega \in \mathbb{R}} \|Q(j\omega)\|$. \mathcal{RH}_∞ is the space of real-rational functions in \mathcal{H}_∞ . It should be clear whether we are considering scalar or matrix-valued functions, but sometimes we will write, say, $\mathcal{H}_\infty^{m \times n}$. For a normed space \mathcal{X} , $\mathcal{B}\mathcal{X}$ denotes its open unit ball. A function in \mathcal{H}_∞ (\mathcal{RH}_∞) is a unit if its inverse also belongs to \mathcal{H}_∞ (\mathcal{RH}_∞).

Signals are represented with lower-case letters and their Laplace transforms are just the same letters with hats. A transfer matrix with input signal u and output signal v is sometimes denoted as $u \mapsto v$. Scalar constants and functions are represented, respectively, by regular and boldface lower-case letters, while matrix constants and matrix-valued functions are assigned, respectively, regular and boldface upper-case letters.

II. A LEFT-COPRIME FACTORIZATION OF LFSS DYNAMICS

We start with an undamped FE model of LFSS dynamics in physical coordinates. This model essentially consists of a constant positive definite mass matrix M and a constant positive semidefinite stiffness matrix K which are used to express the dynamics as

$$M\ddot{q} + Kq = B_0 u \quad (1)$$

$$y = C_0 q \quad (2)$$

where $q(t) \in \mathbb{R}^{n_{\text{FE}}}$ is a vector of attitude coordinates for the rigid part and physical coordinates (displacements and rotations) of the flexible parts of the LFSS, the input $u(t) \in \mathbb{R}^m$ is a vector of actuator forces and torques applied to the structure, and $y(t) \in \mathbb{R}^p$ is the vector of measured outputs (attitude angles, displacements, rotations).

A mode shape matrix E of the structure can be computed from the matrices M and K as follows: Let \hat{E} be a diagonalizing matrix of eigenvectors of $M^{-1}K$, that is, $\hat{E}^{-1}M^{-1}K\hat{E} = \Lambda$. Then \hat{E} also diagonalizes M [10, Theorem 4.5.15 II(b)]: $\hat{E}^T M \hat{E} = F$, where F is a nonsingular diagonal matrix. Let $F^{1/2}$ be the square root of F and finally form $E := \hat{E}(F^{1/2})^{-1}$. This matrix defines a transformation from modal to physical coordinates of the structure. Applying this transformation to (1) and (2), i.e., premultiplying (1) by E^T and substituting $q = E\eta$ in these equations, where η are the modal coordinates, we obtain the dynamic model expressed in modal coordinates.

Then, the model is reduced to a reasonable order by discarding the less significant flexible modes according to some measure of their input–output influence [16]. The first three modes are the rigid-body modes. The modal frequencies of the $n - 3$ retained flexible modes, $\{\omega_i\}_{i=4}^n$, are given by the FE model; uncertainties will be introduced later.

Damping is added to the nominal model since flexibilities in any LFSS are dissipative in nature. So if $\{\bar{\zeta}_i\}_{i=4}^n$ are positive upper bounds and $\{\underline{\zeta}_i\}_{i=4}^n$ nonnegative lower bounds on the otherwise unknown damping ratios, we may take

$\{\zeta_i := (\underline{\zeta}_i + \bar{\zeta}_i)/2\}_{i=4}^n$ as the nominal ones. Thus, adding a diagonal damping matrix D , we get the nominal dynamic equations in modal coordinates η

$$\ddot{\eta} + D\dot{\eta} + \Lambda\eta = B_1 u \quad (3)$$

$$y = C_1 \eta \quad (4)$$

where

$$D = \text{diag}\{0, 0, 0, 2\zeta_4\omega_4, \dots, 2\zeta_n\omega_n\}$$

$$\Lambda = \text{diag}\{0, 0, 0, \omega_4^2, \dots, \omega_n^2\}$$

$$B_1 \in \mathbb{R}^{n \times m}, \quad C_1 \in \mathbb{R}^{p \times n}.$$

Taking Laplace transforms with zero initial conditions yields

$$\hat{\eta}(s) = [s^2 I + sD + \Lambda]^{-1} B_1 \hat{u}(s) \quad (5)$$

$$\hat{y}(s) = C_1 \hat{\eta}(s), \quad (6)$$

The assumptions here are as follows: A1) The sensors have no dynamics. A2) No pole-zero cancellation at $s = 0$ occurs when the product $C_1 [s^2 I + sD + \Lambda]^{-1} B_1$ is formed. A3) The uncertainty in the output matrix C_1 can be lumped in with the input uncertainty. The motivation behind assumptions A1) and A3) is that space sensors are usually accurate and fast while space actuators, which include torque wheels and gas jet thrusters, may add quite a bit of uncertainty in the torque and force inputs. Assumption A2) is standard and just says that the unstable rigid-body modes must be controllable and observable with the set of actuators and sensors used.

Consider the matrix $[s^2 I + sD + \Lambda]$ in (5). It is diagonal, so its inverse is simply

$$[s^2 I + sD + \Lambda]^{-1} = \text{diag} \left\{ \frac{1}{s^2}, \frac{1}{s^2}, \frac{1}{s^2}, \frac{1}{s^2 + 2\zeta_4\omega_4 s + \omega_4^2}, \dots, \frac{1}{s^2 + 2\zeta_n\omega_n s + \omega_n^2} \right\}. \quad (7)$$

Introduce a polynomial $s^2 + as + b$, Hurwitz with real zeros, and form the matrices $\tilde{\mathbf{M}}(s)$, $\tilde{\mathbf{N}}(s)$ as follows:

$$\tilde{\mathbf{M}}(s) := \frac{1}{s^2 + as + b} \text{diag} \{s^2, s^2, s^2, s^2 + 2\zeta_4\omega_4 s + \omega_4^2, \dots, s^2 + 2\zeta_n\omega_n s + \omega_n^2\} \quad (8)$$

$$\tilde{\mathbf{N}}(s) := \frac{1}{s^2 + as + b} B_1. \quad (9)$$

The complex argument s is dropped hereafter to ease the notation. Note that $\tilde{\mathbf{M}}$ and $\tilde{\mathbf{N}}$ belong to \mathcal{RH}_∞ , and the transfer function matrix from \hat{u} to $\hat{\eta}$ is $\mathbf{G} := \tilde{\mathbf{M}}^{-1}\tilde{\mathbf{N}}$, i.e., $\tilde{\mathbf{M}}$ and $\tilde{\mathbf{N}}$ form a left factorization of \mathbf{G} in \mathcal{RH}_∞ . It is easy to show that $\tilde{\mathbf{M}}$ and $\tilde{\mathbf{N}}$ are left-coprime.

III. UNCERTAINTY MODELING FOR LFSS

Uncertainty in FE models is usually characterized by uncertainty in the modal parameters $\{\zeta_i\}_{i=4}^n$ and $\{\omega_i\}_{i=4}^n$, in the mode gains, and in the mode shape matrix E . The uncertainty modeling process proposed here uses the *a priori* knowledge of the bounds for $\{\zeta_i\}_{i=4}^n$, $\{\omega_i\}_{i=4}^n$. For example, the structure designer might say with good certainty that the second mode

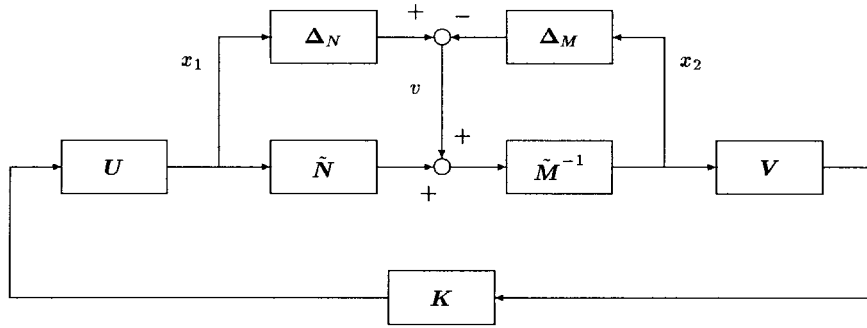


Fig. 1. Feedback control of a perturbed LCF model.

has natural frequency between, say, 0.01 and 0.013 rad/s, and that its damping ratio ζ is almost surely less than 0.05. This information is used to derive a bound on the norm of the coprime factor perturbations at each frequency, which will be needed in the design process for robustness issues. Of course, some uncertainty is also present in the mode shape matrix E of the structure and will be accounted for as uncertainty in the entries of B_1 .

This section can be outlined as follows. First we start with the parametric uncertainty model (11); this induces stable perturbations in \tilde{M} and \tilde{N} . These induced perturbations and their corresponding perturbed factors are given the subscript “ rp ” for *real parameters*. On the other hand, some of the results stated apply to more general perturbations in \mathcal{RH}_∞ , but then the subscript is dropped.

Two scalings are performed on \tilde{M}_{rp} and \tilde{N}_{rp} so that the perturbations are better balanced. Finally, a third scaling normalizes the combined factor perturbations.

It is desired to lump the uncertainty in the mode frequencies, damping ratios, and mode gains into unstructured uncertainty in the coprime factors such that the perturbed LCF of G can be written as

$$G_p = (\tilde{M} + \Delta_M)^{-1}(\tilde{N} + \Delta_N) \quad (10)$$

with $\Delta_M, \Delta_N \in \mathcal{RH}_\infty$. Perturbations in the modal parameters and the entries of B_1 are assumed bounded by nonnegative numbers as follows:

$$|\delta_{\omega_i}| \leq l_{\omega}^i, |\delta_{\zeta_i}| \leq l_{\zeta}^i, |\delta_{b_{ij}}| \leq l_b^{ij} \\ i = 1, \dots, n, j = 1, \dots, m. \quad (11)$$

The following matrices will be useful later on:

$$\Delta_{B_1} := \begin{bmatrix} \delta_{b_{11}} & \cdots & \delta_{b_{1m}} \\ \vdots & \ddots & \vdots \\ \delta_{b_{n1}} & \cdots & \delta_{b_{nm}} \end{bmatrix}, \\ L_B := \begin{bmatrix} l_b^{11} & \cdots & l_b^{1m} \\ \vdots & \ddots & \vdots \\ l_b^{n1} & \cdots & l_b^{nm} \end{bmatrix}.$$

Unmodeled modes, usually (but not necessarily) occurring at high frequencies, can be handled by adjusting the norm bound on the factor uncertainty (though not necessarily at high frequencies only). This can be done iteratively: Design a controller using the technique discussed in this paper and

test it on a set of perturbed full-order evaluation models. If all closed loops are stable (while achieving some desired performance level in the robust performance case), stop—the controller is satisfactory. If not, increase the norm bound on factor uncertainty and redesign the controller.

Perturbations of the coprime factors resulting from perturbations of the real parameters only are easily computed: The perturbed factor \tilde{M}_{rp} is defined as

$$\tilde{M}_{rp} := \tilde{M} + \Delta_{M_{rp}} \quad (12)$$

where we have

$$\Delta_{M_{rp}} := \text{diag} \left\{ 0, 0, 0, \frac{[2\zeta_4 \delta_{\omega_4} + 2\delta_{\zeta_4}(\omega_4 + \delta_{\omega_4})]s + 2\omega_4 \delta_{\omega_4} + \delta_{\omega_4}^2}{s^2 + as + b}, \right. \\ \left. \dots, \frac{[2\zeta_n \delta_{\omega_n} + 2\delta_{\zeta_n}(\omega_n + \delta_{\omega_n})]s + 2\omega_n \delta_{\omega_n} + \delta_{\omega_n}^2}{s^2 + as + b} \right\} \quad (12a)$$

and the perturbed factor \tilde{N}_{rp} is defined as

$$\tilde{N}_{rp} := \tilde{N} + \Delta_{N_{rp}} \quad (13)$$

where $\Delta_{N_{rp}} := \Delta_{B_1}/(s^2 + as + b)$. Now let us consider closed-loop stability of the system in Fig. 1, where a controller K is connected as a feedback around a perturbed LCF, with U and V arbitrary transfer matrices such that no pole-zero cancellation occurs in $\bar{\mathcal{C}}_+$ when the product $V(\tilde{M} + \Delta_M)^{-1}(\tilde{N} + \Delta_N)U$ is formed. Define the uncertainty matrix $\Delta := [\Delta_N \quad -\Delta_M]$. Clearly, if $\Delta_{M_{rp}}$ and $\Delta_{N_{rp}}$ are substituted in this definition, the resulting Δ_{rp} belongs to \mathcal{RH}_∞ . Define the uncertainty set

$$\mathcal{D}_r := \{\Delta \in \mathcal{RH}_\infty : \|\mathbf{r}^{-1}\Delta\|_\infty < 1\} \quad (14)$$

where \mathbf{r} is a unit in \mathcal{H}_∞ (thus the uncertainty is linear time-invariant).

The small-gain theorem yields the following slightly modified result of [18] (see also [14]): The closed-loop system of Fig. 1 with controller K is internally stable for every $\Delta \in \mathcal{D}_r$ iff

- 1) K internally stabilizes VGU ;
- 2) $\|\mathbf{r}(v \mapsto \begin{bmatrix} x_1 \\ x_2 \end{bmatrix})\|_\infty \leq 1$.

Given the parametric uncertainty in (11), a bound of the type $\|\mathbf{r}(j\omega)\|$ that would tightly cover $\|\Delta_{rp}(j\omega)\|$ must be found. But before this weighting function is constructed, different scalings must be performed on the factors and their perturbations to avoid any undue conservativeness and to

“balance” the perturbations, i.e., to minimize the difference between the ∞ -norms of $\Delta_{N_{rp}}$ and $\Delta_{M_{rp}}$.

The first scaling aims at making the components of the rows and columns of B_1 have the same order of magnitude. Let β_j denote the ∞ -norm of the j th column of B_1 and form $J_2 := \text{diag}\{\beta_1, \dots, \beta_m\}$. Now let α_i denote the ∞ -norm of the i th row of $B_1 J_2^{-1}$ and form $J_1 := \text{diag}\{\alpha_1, \dots, \alpha_n\}$. Let $\gamma := \|J_1^{-1} L_B J_2^{-1}\|$ and define the scaled matrices $B_{sc} := \gamma^{-1} J_1^{-1} B_1 J_2^{-1}$ and $\Delta_{B_{sc}} := \gamma^{-1} J_1^{-1} \Delta_{B_1} J_2^{-1}$. It is easy to show that for all Δ_{B_1} satisfying the inequalities in (11), $\|\Delta_{B_{sc}}\| \leq 1$. Finally, we can define the scaled factor and its perturbation

$$\begin{aligned} \tilde{N}_0 &:= b\gamma^{-1} J_1^{-1} \tilde{N} J_2^{-1} \\ &= (s^2 + as + b)^{-1} b B_{sc} \end{aligned} \quad (15)$$

$$\begin{aligned} \Delta_{N_{rp0}} &:= b\gamma^{-1} J_1^{-1} \Delta_{N_{rp}} J_2^{-1} \\ &= (s^2 + as + b)^{-1} b \Delta_{B_{sc}}. \end{aligned} \quad (16)$$

The second scaling is performed on \tilde{M} to make sure that the norm of any perturbation of it induced by variations in the modal parameters is less than or equal to one, but close to one at low frequencies. Let $c_i := 2\zeta_i l_\omega^i + 2l_\omega^i (\omega_i + l_\omega^i)$ and $d_i := 2\omega_i l_\omega^i + l_\omega^i$ for $i = 4, \dots, n$. These constants are the coefficients of the numerator of the (i, i) entry of $\Delta_{M_{rp}}$ when all modal perturbations are replaced by their upper bounds. Letting $c_{\max} := \max_{i=4, \dots, n} c_i$ and $d_{\max} := \max_{i=4, \dots, n} d_i$, we can now define the second scaled factor and its perturbation

$$\tilde{M}_0 := \frac{b}{d_{\max}} \tilde{M} \quad (17)$$

$$\Delta_{M_{rp0}} := \frac{b}{d_{\max}} \Delta_{M_{rp}}. \quad (18)$$

These two scalings are illustrated in Fig. 2 by a sequence of block diagrams showing the transformations performed on the coprime factors and their perturbations. We have included a block for the diagonal transfer matrix T_a that models actuator dynamics. Note that the properties of linearity and commutativity of diagonal matrices are used in order to move blocks around and get the desired final block diagram. Also note that \tilde{N}_0 and \tilde{M}_0 are still coprime. It is our experience that these types of scalings help a lot in reducing the \mathcal{H}_∞ norm of the generalized plant’s weighted transfer matrix in an actual design. The last scaling performed on the perturbation $\Delta_{rp0} := [\Delta_{N_{rp0}} \quad -\Delta_{M_{rp0}}]$ normalizes it with the weighting function $\mathbf{r}(s)$ to get $\|\hat{\Delta}_{rp0}\|_\infty < 1$. This is illustrated in Fig. 3 where T_a models actuator dynamics.

We are now ready to design a weighting function $\mathbf{R} = \mathbf{r}I$ for the scaled perturbation Δ_{rp0} . In so doing, the freedom provided by coefficients of the common denominator $s^2 + as + b$ will be used to our advantage to keep the order of \mathbf{r} as low as possible without paying the price of added conservativeness. Here is the result proved in the Appendix.

Proposition 1: For $k > 0$, define a and b via $s^2 + as + b := [s + (d_{\max}/c_{\max})](s + k)$ and let $\mathbf{r}(s) := [(\epsilon_1 s + \sqrt{2} + \epsilon_0)/(s/k + 1)]$, where ϵ_0 and ϵ_1 are small positive numbers. Then $\|\mathbf{r}^{-1} \Delta_{rp0}\|_\infty < 1$.

This weighting function is of first order, which is a benefit considering that it will be duplicated $m + n$ times in

the generalized plant of Fig. 4. By construction, for small ϵ_0, ϵ_1 , $|\mathbf{r}(j\omega)|$ is a relatively tight bound on $\|\Delta_{rp0}(j\omega)\|$, especially at low and high frequencies. With the unit \mathbf{r} given by Proposition 1, the factor perturbation Δ_{rp0} belongs to the uncertainty set \mathcal{D}_r and the normalized $\hat{\Delta}_{rp0}$ belongs to $\mathcal{BRH}_\infty^{n \times (m+n)}$. Now introduce a normalized scaled perturbation $\hat{\Delta}_0 \in \mathcal{BRH}_\infty^{n \times (m+n)}$. Then letting $\Delta_0 := \mathbf{r} \hat{\Delta}_0$, one obtains that Δ_0 is an arbitrary element in \mathcal{D}_r . In this way \mathbf{r} can be included in the generalized plant of Fig. 4. This figure shows the scaled closed-loop system with all the weights for designing a controller \mathbf{K} providing robust stability and nominal performance.

IV. ROBUST \mathcal{H}_∞ DESIGN

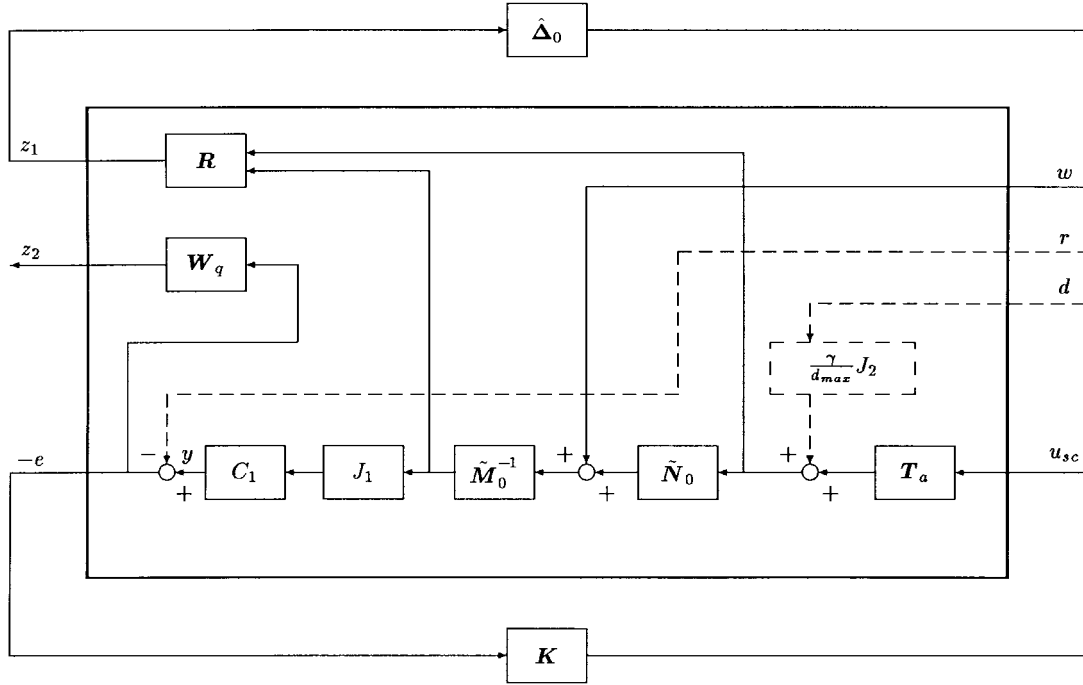
According to the necessary and sufficient condition for robust stability of perturbed coprime factorizations stated in Section III, our robust stability objective will be to minimize $\|w \mapsto z_1\|_\infty$ to a value no more than one over all stabilizing controllers. Now consider the problems of attitude regulation and vibration attenuation. For these problems, it makes sense to ask for good torque/force disturbance rejection at low frequencies as a first requirement for nominal performance. For example, this may be required on a flexible space station on which there may be large robots or humans producing significant torque disturbances. As a second requirement for nominal performance, we will ask for good tracking of reference angle trajectories to allow accurate slewing maneuvers of the rigid part of the structure.

Referring to Fig. 4, these requirements can be translated into desired shapes for the norms of the sensitivity functions $\mathbf{S}_{rh} := r \mapsto e_h$ and $\mathbf{S}_{dh} := d \mapsto y_h$, where r is the vector of input references, e_h is the vector of attitude angle errors for the rigid part of the structure (the h subscript stands for *hub*, the rigid part of Daisy), d is the vector of external torque/force disturbances, and $y_h = [\theta_{hx} \theta_{hy} \theta_{hz}]^T$ is the vector of attitude angles of the rigid part. Note that if we define $\mathbf{S}_r := r \mapsto e$, where e is the vector of all position/angle errors, and $\mathbf{S}_d := d \mapsto y$, then $\mathbf{S}_{rh} = [I_{3 \times 3} 0_{3 \times (p-3)}] \mathbf{S}_r$ and $\mathbf{S}_{dh} = [I_{3 \times 3} 0_{3 \times (p-3)}] \mathbf{S}_d$. These frequency-domain specifications are well suited for the \mathcal{H}_∞ design method [8] or a μ -synthesis [2]. Here we discuss the \mathcal{H}_∞ approach.

The block diagram of Fig. 4 shows the interconnections between the scaled factors and their perturbations, actuator dynamics, scaling and output matrices, controller, and weighting functions that form the controlled perturbed generalized plant used in the \mathcal{H}_∞ design. The weighting function \mathbf{W}_q will allow us to shape the sensitivity functions as desired.

If we define v as the input to the actuator dynamics transfer matrix, then the input signal u_{sc} is just a scaled version of the physical signal v : $u_{sc} := (\gamma/d_{\max}) J_2 v$. A few algebraic computations done on the system of Fig. 4 show that $\mathbf{S}_r := (I - C_1 J_1 \tilde{M}_0^{-1} \tilde{N}_0 T_a \mathbf{K})^{-1}$ and $\mathbf{S}_d := (\gamma/d_{\max}) \mathbf{S}_r C_1 J_1 \tilde{M}_0^{-1} \tilde{N}_0 J_2$. For $q > 0$, let $\mathbf{W}_q := q\mathbf{w}[I_{3 \times 3} 0_{3 \times (p-3)}]$, and let $\mathbf{W}_1 := \mathbf{W}_q|_{q=1}$.

We consider the following problem of robust stability and nominal performance. It is desired to reduce the ∞ -norm of the transfer matrix $\mathbf{W}_1 \mathbf{S}_d$ to a value less than or equal to one

Fig. 4. Generalized plant with scaled perturbation and controller for \mathcal{H}_∞ design.

to achieve $\|\mathcal{S}_{dh}(j\omega)\| \leq |w^{-1}(j\omega)|$, $\forall \omega$ for good force/torque disturbance rejection at low frequencies. As a second requirement, we would like to keep the norm of $\mathcal{S}_{rh}(j\omega)$ smaller than $|w^{-1}(j\omega)|$ to achieve good low-frequency input tracking. These specifications lead to the following *robust stability and nominal performance* problem.

Problem RSNP: Design a finite-dimensional, proper, linear time-invariant controller \mathbf{K} such that, with $q = 1$ and $\hat{\Delta}_0 \equiv 0$, the closed-loop system has the following properties:

- 1) $\|w \mapsto z_1\|_\infty \leq 1$ (robust stability);
- 2) $\|r \mapsto z_2\|_\infty \leq 1$;
- 3) $\|d \mapsto z_2\|_\infty \leq 1$.

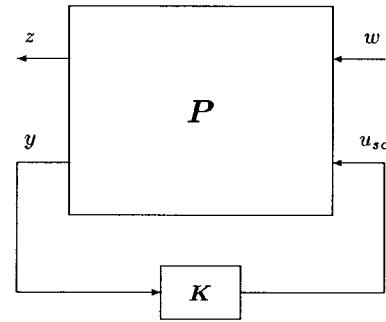
Note that the reference and torque/force disturbance input channels labeled, respectively, r and d , and represented by dashed lines in Fig. 4, are not included in the design process. This is to avoid introducing too many cross terms in the closed-loop transfer matrix whose ∞ -norm is to be minimized. Thus, a compromise standard \mathcal{H}_∞ problem is set up to solve Problem RSNP. The basic goal of the proposed \mathcal{H}_∞ design is to achieve $\|w \mapsto \begin{bmatrix} z_1 \\ z_2 \end{bmatrix}\|_\infty \leq 1$ for $\hat{\Delta}_0 \equiv 0$.

The \mathcal{H}_∞ design method minimizes the ∞ -norm of the closed-loop map $w \mapsto z$ over all stabilizing controllers in Fig. 5, where $z := \begin{bmatrix} z_1 \\ z_2 \end{bmatrix}$. The design block diagram of Fig. 5 represents the same system as the one in Fig. 4 but without the perturbation $\hat{\Delta}_0$ and the exogenous signals r and d . The generalized design plant \mathbf{P} is given by

$$\mathbf{P} := \begin{bmatrix} \mathbf{P}_{11} & \mathbf{P}_{12} \\ \mathbf{P}_{21} & \mathbf{P}_{22} \end{bmatrix} \quad (19)$$

where

$$\mathbf{P}_{11} := \begin{bmatrix} 0 \\ r\tilde{\mathbf{M}}_0^{-1} \\ \mathbf{W}_q \mathbf{C}_1 \mathbf{J}_1 \tilde{\mathbf{M}}_0^{-1} \end{bmatrix}$$

Fig. 5. Generalized plant for \mathcal{H}_∞ design.

$$\mathbf{P}_{12} := \begin{bmatrix} r\tilde{\mathbf{T}}_a \\ r\tilde{\mathbf{M}}_0^{-1}\tilde{\mathbf{N}}_0\tilde{\mathbf{T}}_a \\ \mathbf{W}_q \mathbf{C}_1 \mathbf{J}_1 \tilde{\mathbf{M}}_0^{-1}\tilde{\mathbf{N}}_0\tilde{\mathbf{T}}_a \end{bmatrix}$$

$$\mathbf{P}_{21} := \mathbf{C}_1 \mathbf{J}_1 \tilde{\mathbf{M}}_0^{-1}$$

$$\mathbf{P}_{22} := \mathbf{C}_1 \mathbf{J}_1 \tilde{\mathbf{M}}_0^{-1}\tilde{\mathbf{N}}_0\tilde{\mathbf{T}}_a.$$

Problem COMP: Design a finite-dimensional, proper, linear time-invariant controller \mathbf{K} such that for $\hat{\Delta}_0 \equiv 0$, the nominal closed loop of Fig. 5 achieves $\|w \mapsto z\|_\infty \leq 1$.

Justification that a solution to Problem COMP also solves Problem RSNP is given by Proposition 2 which, more specifically, states that we can shape the norms of \mathcal{S}_{dh} and \mathcal{S}_{rh} indirectly by minimizing $\|w \mapsto z_2\|_\infty$ (the proof is in the Appendix). Referring to Fig. 4 again, let $\mathbf{S}_1 := (\mathbf{I} - \tilde{\mathbf{M}}_0^{-1}\tilde{\mathbf{N}}_0\tilde{\mathbf{T}}_a\mathbf{K}\mathbf{C}_1\mathbf{J}_1)^{-1}$. In the sequel, fix $k = c_{\max}/d_{\max}$ in the second-order common denominator of the scaled factors.

Proposition 2: Assume \mathbf{C}_1 is right invertible and let \mathbf{C}_1^\dagger be a right inverse of \mathbf{C}_1 . Let $q := \max\{\|\tilde{\mathbf{M}}_0\mathbf{J}_1^{-1}\mathbf{C}_1^\dagger\|_\infty, d_{\max}^{-1}\|\mathbf{J}_1^{-1}\mathbf{B}_1\|\}$. If the controller \mathbf{K} is

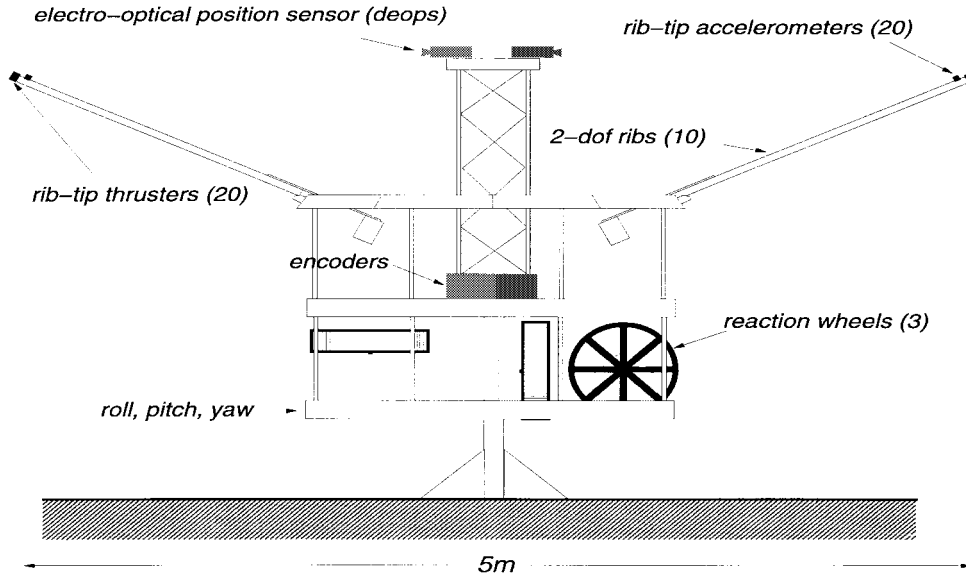


Fig. 6. Daisy LFSS experimental testbed.

internally stabilizing and achieves

$$\left\| w \mapsto \begin{bmatrix} z_1 \\ z_2 \end{bmatrix} \right\|_{\infty} = \left\| \begin{bmatrix} \mathbf{r} \mathbf{T}_a \mathbf{K} \mathbf{C}_1 \mathbf{J}_1 \mathbf{S}_1 \tilde{\mathbf{M}}_0^{-1} \\ \mathbf{r} \mathbf{S}_1 \tilde{\mathbf{M}}_0^{-1} \\ \mathbf{W}_q \mathbf{S}_r \mathbf{C}_1 \mathbf{J}_1 \tilde{\mathbf{M}}_0^{-1} \end{bmatrix} \right\|_{\infty} \leq 1 \quad (20)$$

then the closed-loop system of Fig. 4 is robustly stable to all perturbations $\hat{\Delta}_0 \in \mathcal{BRH}_{\infty}^{m \times (m+n)}$, and for every $\omega \in \mathbb{R}$ we have

$$\|\mathbf{S}_{dh}(j\omega)\| \leq |\mathbf{w}^{-1}(j\omega)| \quad (21)$$

$$\|\mathbf{S}_{rh}(j\omega)\| \leq |\mathbf{w}^{-1}(j\omega)|. \quad (22)$$

The choice of q in Proposition 2 may be used for a first design to get insight into the tradeoff between robustness and performance, but smaller values of q may be tried to reach a satisfactory design achieving (21) and (22). In our experiments on Daisy, we found that weighting all the outputs was asking too much given the uncertainty in the model and the actuator saturation levels. Hence, only the hub angles were weighted with \mathbf{W}_q as above. In any case, the modal coordinates are weighted by \mathbf{r} (see Fig. 4), which in our experiments on Daisy resulted in sufficient vibration attenuation.

To recap, if a stabilizing \mathbf{K} satisfying (20) has been designed, it follows that 1) \mathbf{K} provides robust stability to all perturbations of the modal parameters satisfying (11) and 2) \mathbf{K} provides nominal performance in the sense that inequalities (21) and (22) hold. Note that the controller \mathbf{K}_p to be implemented on the real system is a scaled version of \mathbf{K} , i.e., $\mathbf{K}_p = (d_{\max}/\gamma) \mathbf{J}_2^{-1} \mathbf{K}$.

A. \mathcal{H}_{∞} Designs for Daisy

Daisy [6] is an experimental testbed built at the University of Toronto Institute for Aerospace Studies (UTIAS) whose dynamics are meant to approximate those of real LFSS; see Fig. 6. It consists of a rigid hub (the ‘‘stem’’) mounted on a spherical joint and on top of which are ten ribs (the ‘‘petals’’) attached through passive two-degree-of-freedom rotary joints

and low-stiffness springs. Each rib is coupled to its two neighbors via low-stiffness springs. The hub represents the rigid part of the LFSS, while the ribs model the flexibilities in the LFSS. Each rib is equipped with four unidirectional air jet thrusters that are essentially on-off devices, each capable of delivering a torque of 0.8 Nm at the rib joint. Pulse-width modulation (PWM) of the thrust is used to apply desired torques on the ribs. The four thrusters are aligned by pairs to implement two orthogonal bidirectional actuators. So from now on, when we use the word thruster alone, we will mean *bidirectional* thruster.

Mounted at the tip of each rib is an infra-red emitting diode. Two hub-mounted infra-red CCD cameras measure the positions of these diodes via ten lenses, and the rib angles are computed from these measurements. This electro-optical system called DEOPS was developed at UTIAS [12]. The hub actuators consist of three torque wheels driven by DC motors whose axes are orthogonal. Each can deliver up to 58 Nm but is limited to 38.8 Nm. The hub orientation and angular velocity can be measured with position and velocity encoders. For this research, only DEOPS and the hub position encoders were used as sensors.

The dynamic model available for Daisy is of 46th order, including 20 flexible modes with nominal frequencies ranging from approximately 0.56 to 0.71 rad/s and damping ratios from 0.015 to 0.06. Open-loop experiments showed that the uncertainty in the modal frequencies is roughly 10%, while damping ratios are accurate only to within 50%. Some of the modes are multiple. Two of the rigid-body modes are pendulous, so they can be considered as flexible modes; they both have frequency 0.29 ± 0.03 rad/s and their damping ratios are 0.11 ± 0.05 and 0.09 ± 0.05 . The model has the form of (3). Note that Daisy is not ‘‘easy’’ to control: Collocated \mathcal{H}_2 controllers designed without robustness considerations and implemented on Daisy failed to stabilize it. The method described in Section IV is illustrated by designing a robust controller for collocated and

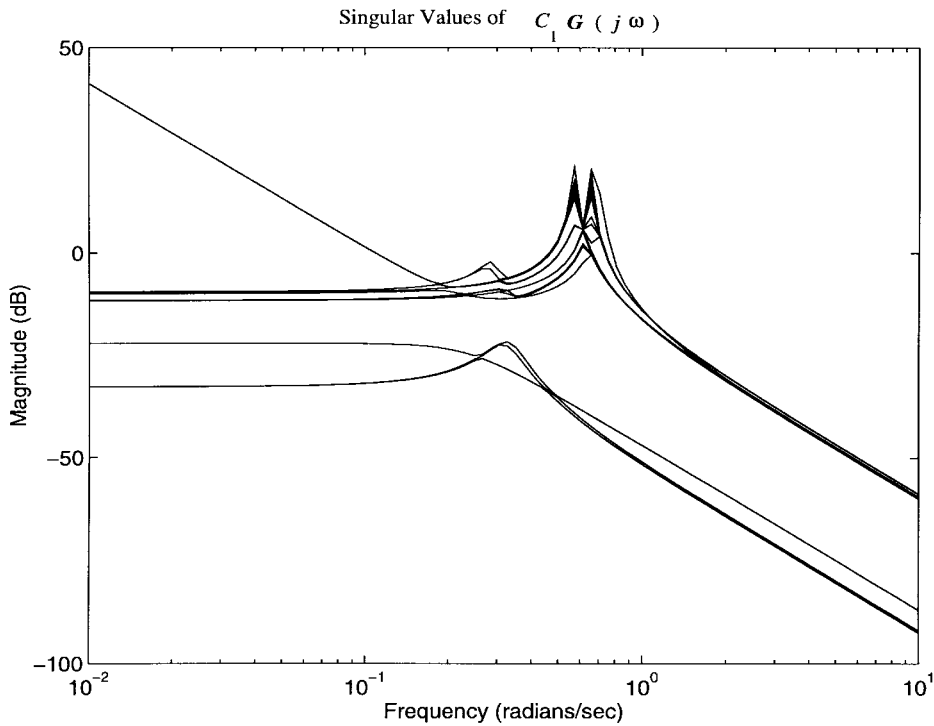


Fig. 7. Singular values of $C_1\mathbf{G}(j\omega)$.

noncollocated configurations of Daisy using the \mathcal{H}_∞ design method.

1) *Collocated Case*: By collocation we mean that all rotations and displacements produced by the actuators at their locations are measured and that each sensor has a corresponding collocated actuator. Thus 23 actuator/sensor pairs are used, namely the 20 bidirectional rib thrusters with the DEOPS system measuring the 20 rib angles, plus the three hub reaction wheels with the three corresponding angle encoders.

In terms of system equations (3) and (4), the inputs are $u = [\tau_{hx}\tau_{hy}\tau_{hz}\tau_{r1}\tau_{r2}\cdots\tau_{r20}]^T$, where the first three are the hub torques around the x , y , and z axes, and the last 20 inputs are the rib torques given by

$$\tau_{ri} = \begin{cases} \text{rib } (i+1)/2 \text{ out-of-cone torque,} & i \text{ odd} \\ \text{rib } i/2 \text{ in-cone torque,} & i \text{ even} \end{cases} \quad (23)$$

where *out-of-cone* and *in-cone* refer to orthogonal directions outside or inside the cone formed by the ten ribs. All torque inputs are expressed in Nm. The input matrix $B_1 \in \mathbb{R}^{23 \times 23}$ is assumed to have up to 8% uncertainty in its entries.

The torque wheels have some dynamics, i.e., for each wheel, the transfer function between the desired and produced torques is first order and strictly proper. On the other hand, the PWM thrusters, which deliver average torques close to the desired ones, are modeled as pure gains. Overall, the transfer matrix \mathbf{T}_a in Fig. 4 is taken to be

$$\mathbf{T}_a = \text{diag} \left\{ \frac{0.01s+1}{0.36s+1}, \frac{0.01s+1}{0.36s+1}, \frac{0.01s+1}{0.36s+1}, 1, 1, \dots, 1 \right\} \quad (24)$$

where the terms $0.01s$ are added in the numerators to regularize the generalized plant for the \mathcal{H}_∞ problem, and the 0.36

time constants were measured experimentally. Note that \mathbf{T}_a commutes with J_2 .

The outputs are the angles $y = [\theta_{hx}\theta_{hy}\theta_{hz}\theta_{r1}\theta_{r2}\cdots\theta_{r20}]^T$, which correspond to the input torques described above. The output matrix is just the mode shape matrix $C_1 = E \in \mathbb{R}^{23 \times 23}$, which is invertible. All angles are expressed in radians. Finally, $\Lambda = \text{diag}\{\omega_1^2, \dots, \omega_{23}^2\}$ and $D = \text{diag}\{2\zeta_1\omega_1, \dots, 2\zeta_{23}\omega_{23}\}$.

A plot of the 23 singular values of $C_1\mathbf{G}(j\omega)$ is shown in Fig. 7. An analysis of the Hankel singular values of a normalized coprime factorization of the plant model $C_1\mathbf{G}$ [15] showed that they all lie between 0.2 and 0.9, which indicates that the model should not be reduced. Consequently, our design model includes all the modes. It is desired to control Daisy's model so that it remains stable for all bounded perturbations of the modal parameters and all perturbations of the entries of B_1 within 8% of their nominal values. We also want good torque/force disturbance rejection and good tracking in the sense of (21) and (22). The generalized plant for the robust \mathcal{H}_∞ design is built according to Fig. 5, and the different constants and weighting functions are

$$\begin{aligned} d_{\max} &= 0.107, \quad c_{\max} = 0.046, \quad k = \frac{c_{\max}}{d_{\max}} = 0.43 \\ \gamma &= 0.79, \quad q = 10^3, \\ \mathbf{w}(s) &= \frac{100}{s^2 + \frac{2 \times 0.7s}{0.01} + 1} \end{aligned} \quad (25)$$

$$\mathbf{r}(s) = \frac{0.001s + 1.415}{2.33s + 1}. \quad (26)$$

Note that $q = 1.42 \times 10^4$ when computed using the formula in Proposition 2, but this value turned out to be too large to

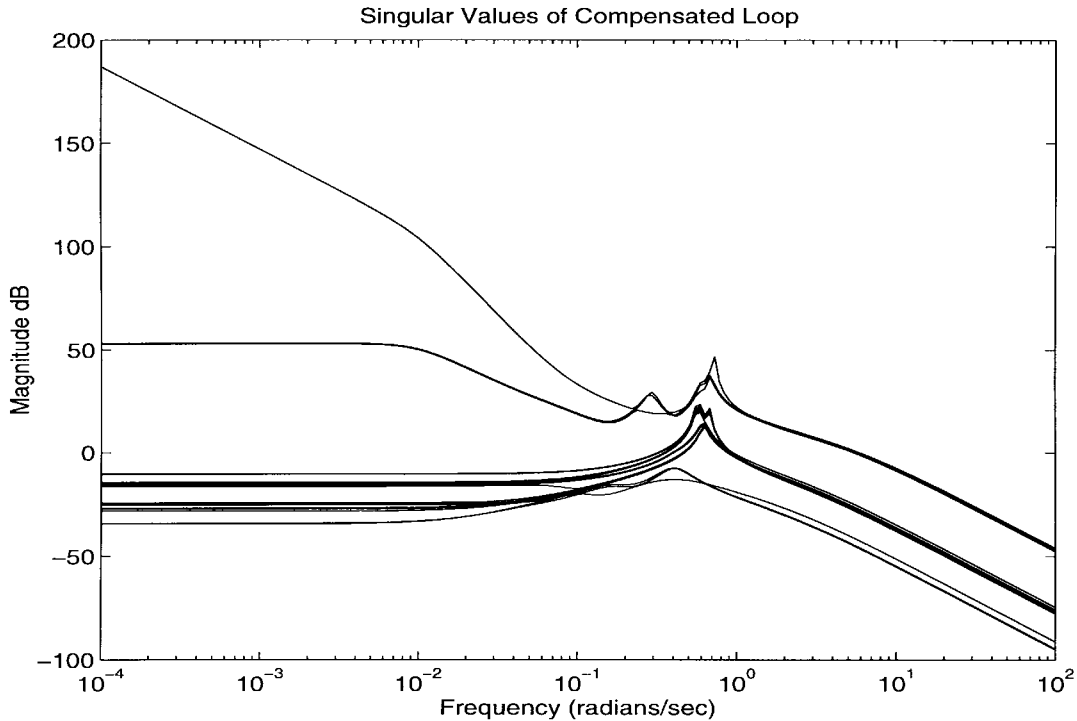


Fig. 8. Singular values of compensated loop $C_1 J_1 \tilde{M}_0^{-1} \tilde{N}_0 T_a K_1$.

get the ∞ -norm of $w \mapsto z$ down to less than one. However, q reduced to 1000 led to a good tradeoff between robustness and performance. Also note that computational delay and zero-order hold models were not included in the generalized plant even though both were present in the digital implementation of the controller on Daisy. It was anticipated that the design would be robust to these unmodeled dynamics; this was borne out by experiments.

No antialiasing analog filters were available to filter the measured hub angle signals, nor for DEOPS signals, which are inherently digital. Even though this is rather undesirable, high-frequency noise levels seemed sufficiently small to avoid serious aliasing problems in the experiments.

The \mathcal{H}_∞ design was carried out in MATLABTM using the μ -ToolsTM [2] command *hinfsyn*, which minimizes the ∞ -norm of the closed-loop map $w \mapsto z$ over all stabilizing controllers in Fig. 5, and computes a suboptimal controller achieving an ∞ -norm within some desired accuracy of the optimal.

The generalized design plant P is given by (19). If a realization of it is obtained using a computer, this realization will in general be nonminimal because pole-zero cancellations might not be carried out. Also note that P is unstable, so one cannot use the balanced truncation method to get rid of the unobservable and uncontrollable modes. Therefore we used the decentralized fixed-mode method [7] to obtain a minimal realization of P , reducing it from 147 to 78 state variables, which equals its McMillan degree. This method has the advantage of being computationally simple and hence more reliable for such large systems. A stable suboptimal controller achieving $\|w \mapsto z\|_\infty = 0.94$ was obtained. Its order was the same as the order of the minimal generalized plant, i.e., 78, but

a balanced truncation reduced it to 55 state variables without affecting the closed-loop ∞ -norm.

A plot of the singular values of the loop $C_1 J_1 \tilde{M}_0^{-1} \tilde{N}_0 T_a K_1$ with this reduced controller K_1 is shown in Fig. 8. It can be seen that the controller does not try to invert the plant: peaks are still present in the plot. Robust stability was achieved with K_1 as $\|w \mapsto z_1\|_\infty = 0.94$, while Fig. 9 shows that the required performance has been attained, i.e., $\|S_{rh}(j\omega)\|$ and $\|S_{dh}(j\omega)\|$ are less than $|w^{-1}(j\omega)|$, as desired. The least-damped closed-loop mode has a damping ratio of 0.38. The 55th-order controller K_1 was rescaled to $K_{p1} = (d_{\max}/\gamma) J_2^{-1} K_1$, a controller using the actual rib and hub angles to compute actual rib and hub control torques. Then, since the implementation of the controller must be digital, K_{p1} was discretized at a sampling rate of 10 Hz using the bilinear transformation; call the resulting controller K_{p1d} . An earlier version of our control program allowed a maximum sampling rate of 5 Hz only—when used to implement a discretized version of K_{p1} , it destabilized the closed loop. This suggests that an \mathcal{H}_∞ -optimal sampled-data design might be warranted here, but this is left for future work.

We used the standardized hub torque disturbance profile in Fig. 10 for all our test experiments and simulations. It can be applied by any of the three torque wheels individually or in any combination. In all the experiments and simulations, the controller is switched on after the hub angle experiencing the largest deviation changes sign. Thus the disturbance has roughly the effect of a torque impulse applied to the hub because the controller starts when the hub angles are small while the angular velocities are large. However, the rib angles may not be small at switch-on time.

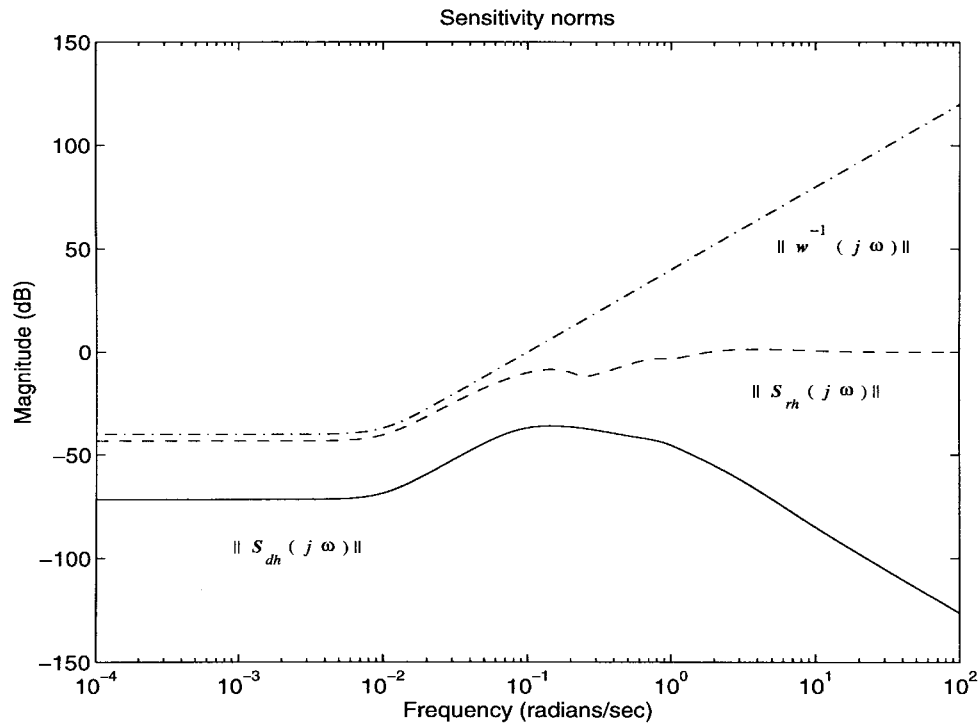


Fig. 9. Norms of $S_{dh}(j\omega)$ and $S_{rh}(j\omega)$ for K_1 .

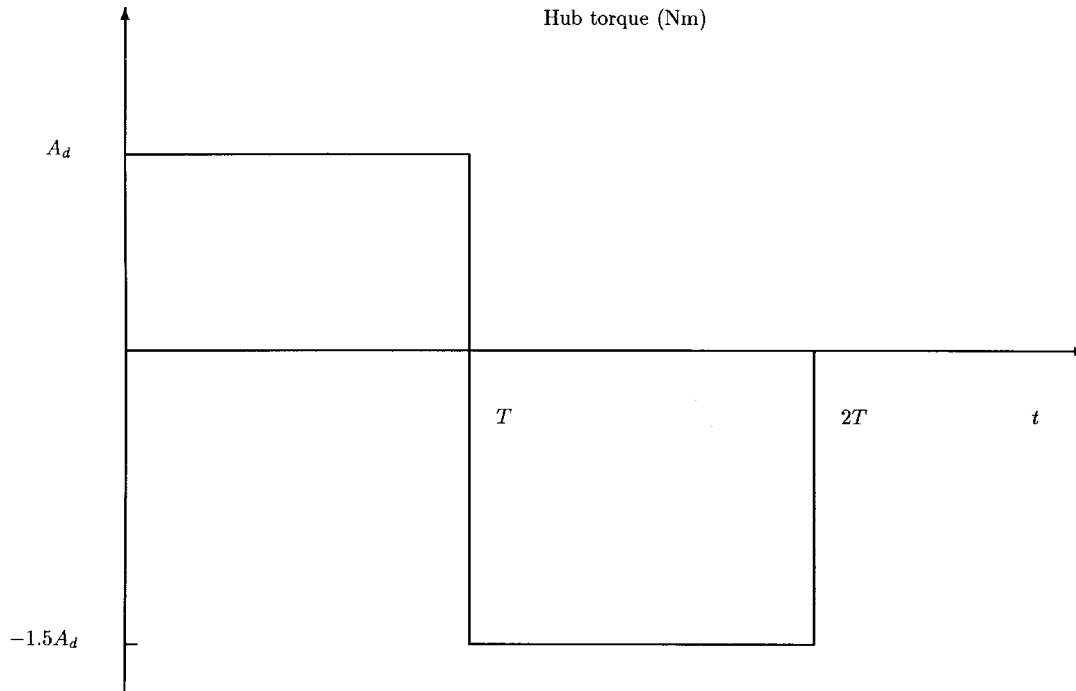


Fig. 10. Standard hub torque disturbance $D(A_d, T, axes)$.

For all the plots, $t = 0$ corresponds to the instant at which the controller is turned on. Most of the analyzes of the experiments will be qualitative, based on the experimental plots. For instance, we will use the expression “settling time” in a loose way, without defining it rigorously.

Before we proceed to present the closed-loop simulation and experimental results, an open-loop response of Daisy

to $D(13.5 \text{ Nm}, 2s, x)$ is plotted in Fig. 11 along with a simulated continuous-time response of the nominal model C_1G . Discrepancies between some of the actual and nominal modal frequencies and damping ratios can be observed from these plots, illustrating the uncertainty in the model. All simulations are linear and *discrete-time* with the plant model (including actuator dynamics) discretized at 10 Hz using the

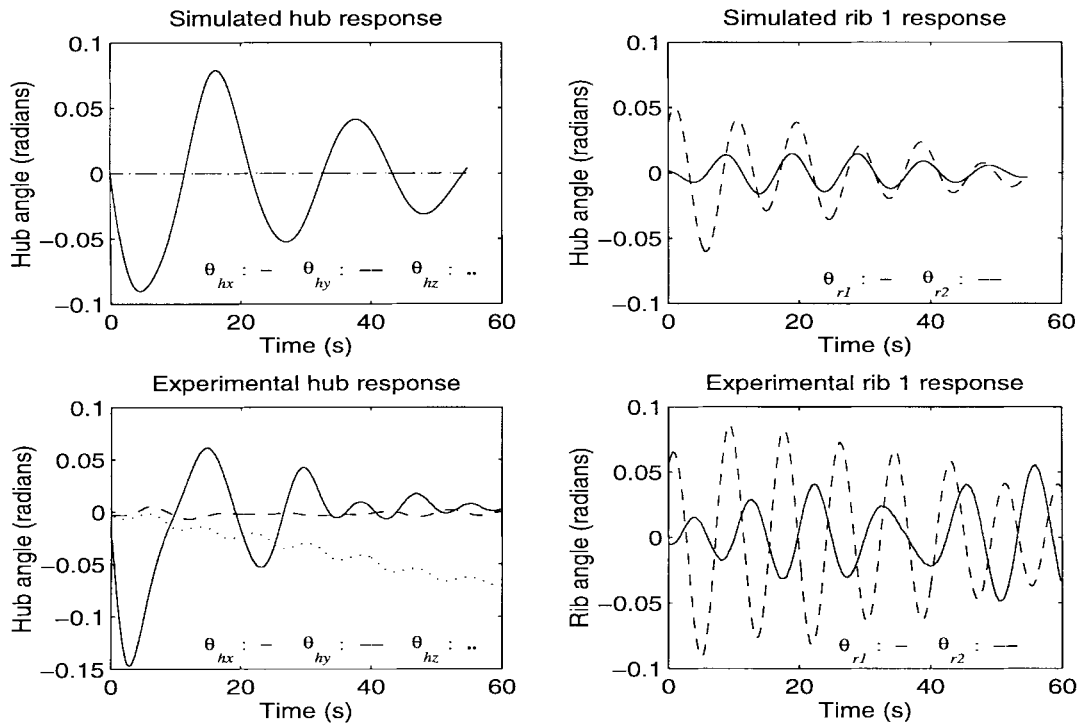


Fig. 11. Simulated and experimental open-loop responses of Daisy to $D(13.5 \text{ Nm}, 2s, x)$.

Matlab function $c2d$, which performs the discretization by placing a sampler at the output of the model and a zero-order hold at the input.

The first closed-loop experiment with K_{p1d} is the response to $D(13.5 \text{ Nm}, 2s, y)$. The simulated and actual hub angles are shown in Fig. 12. Note that absolutely no experimental tuning was necessary to get all the responses in this research, unlike some PD, LQR, and LQG controllers that were previously tested on Daisy. The settling times of the experimental and simulated θ_{hy} are approximately the same but the transient response is much larger experimentally. This is due in part to hub torque saturation. The simulated and experimental *computed* control torques were within their limits except for the first second where saturation occurred. Recall that the saturation levels are 38.8 and 0.8 Nm for the hub and rib torques, respectively, but the simulations do not have these limits. Fig. 13 shows the simulated and actual rib angles. It can be observed from this figure that the experimental rib angles are reasonably close to the simulated ones, even though the experimental computed rib torques were as large as three times the saturation levels for the first few seconds. Finally notice how the experimental rib responses do not converge to zero as rapidly as in the simulation. This is due to a significant deadband in the jet thrusters input-output characteristics. This deadband was not quantified but will be for future experiments.

Results for $D(13.5 \text{ Nm}, 2s, x)$ were less consistent than in the previous case, but still satisfactory. The experimental response to $D(13.5 \text{ Nm}, 2s, z)$ was comparable to the simulated one [4].

2) *Noncollocated Case*: Daisy's actuators and sensors can be combined in many different ways, allowing the study of noncollocated control of LFSS. We chose to use all 23 angle

measurements (DEOPS) but only 17 thrusters and the three hub reaction wheels. The three rib actuators not employed are the in-cone jet thrusters of ribs 2, 5, and 7. Past experiments with noncollocated controller designs based on the available model always destabilized the closed loop, so it was deemed appropriate to improve the model using open-loop data in order to reduce the uncertainty in the modal parameters. This exercise resulted in a new set of modal frequencies with associated estimates of uncertainties: From 0.59 to 0.79 rad/s, all with 5% uncertainty. The B_1 matrix of (3) for this model is a slightly modified version of the one for the previous model with its 7, 13, and 17th columns removed. It is assumed to have up to 5% uncertainty in its entries. The output matrix C_1 is the same as in the previous model. All the modes are retained in the noncollocated nominal design model as the Hankel singular values of a normalized coprime factorization of the new C_1G all lie between 0.17 and 0.92. There are no transmission zeros in $\bar{\mathcal{T}}_+$ in the nominal plant model.

It is desired to control the noncollocated model so that it remains stable for all bounded perturbations of the modal parameters and all perturbations of the entries of B_1 within 5% of their nominal values. We also want good torque/force disturbance rejection in the sense of (21), but a few iterations of the design suggested that we have to relax the tracking requirement (22) in order to achieve robust stability and (21). Hence we will focus only on the disturbance rejection specification. Also, it was found that the uncertainties in the model had to be assumed somewhat smaller than given to guarantee closed-loop internal stability, namely 4% in the entries of B_1 , 3% in the modal frequencies, and 20% in the damping ratios. Note that this does not mean that instability will automatically result if some of the actual modal

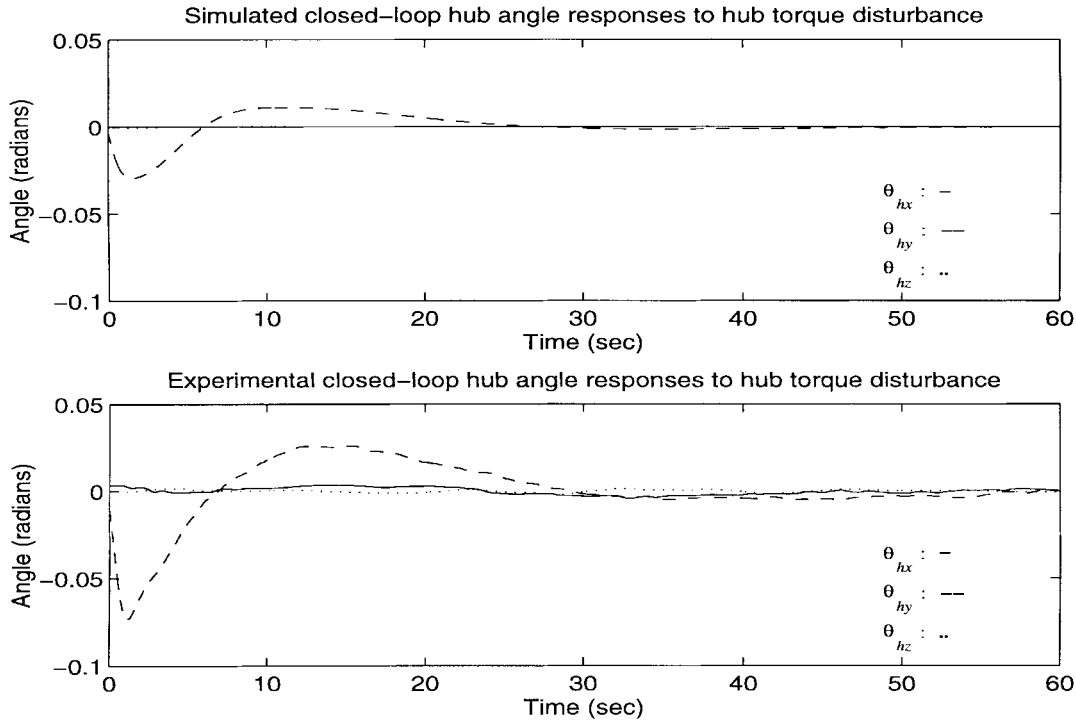


Fig. 12. Simulated and experimental closed-loop hub angle responses with \mathbf{K}_{p1d} , $D(13.5 \text{ Nm}, 2s, y)$.

parameters lie outside those ranges. Indeed inequality (20) is only sufficient, and furthermore there is some conservativeness in the choice of \mathbf{r} given by Proposition 1.

The generalized plant for the robust \mathcal{H}_∞ design is built according to Fig. 5, and the different constants and weighting functions are

$$\begin{aligned} d_{\max} &= 0.038, \quad c_{\max} = 0.018, \quad k = \frac{c_{\max}}{d_{\max}} = 0.47 \\ \gamma &= 0.37, \quad q = 400, \\ \mathbf{w}(s) &= \frac{50}{s^2 + \frac{2 \times 0.7s}{(0.01)^2 + \frac{0.01}{0.01}} + 1} \end{aligned} \quad (27)$$

$$\mathbf{r}(s) = \frac{0.001s + 1.415}{2.1s + 1}. \quad (28)$$

Note that $q = 4 \times 10^4$ when computed using the formula in Proposition 2, but this value was much too large to get the ∞ -norm of $w \mapsto z$ down to less than one. So q was reduced to 400, a satisfactory value obtained after a few iterations of the design procedure.

The \mathcal{H}_∞ design was again carried out in MATLAB. We used the decentralized fixed-mode method [7] to obtain a minimal realization of \mathbf{P} , reducing it from 138 to 75 state variables. A stable suboptimal controller achieving $\|w \mapsto z\|_\infty = 0.62$ was obtained. Its order was the same as the order of the minimal realization of the generalized plant, i.e., 75, but a balanced truncation reduced it to the 49th-order controller \mathbf{K}_2 without affecting the closed-loop ∞ -norm. With this reduced controller \mathbf{K}_2 , robust stability was achieved as $\|w \mapsto z_1\|_\infty = 0.62$ while Fig. 14 shows that the required performance has been attained, i.e., $\|\mathbf{S}_{dh}(j\omega)\|$ is less than $|w^{-1}(j\omega)|$ as desired,

although $\|\mathbf{S}_{rh}(j\omega)\|$ is not as nice as in the previous collocated design. The least-damped closed-loop mode has a damping ratio of 0.18. The 49th-order controller \mathbf{K}_2 was rescaled to $\mathbf{K}_{p2} = (d_{\max}/\gamma)J_2^{-1}\mathbf{K}_2$. Then \mathbf{K}_{p2} was discretized at a sampling rate of 10 Hz using the bilinear transformation; call the resulting controller \mathbf{K}_{p2d} .

The first closed-loop experiment with \mathbf{K}_{p2d} is the response to $D(13.5 \text{ Nm}, 2s, x)$. The simulated and actual hub angles are shown in Fig. 15 while Fig. 16 shows the simulated and actual rib angles. The experimental response of θ_{hx} has a transient about twice as large as in the simulation but the settling times are comparable. However, the experimental rib responses look quite different from the simulated ones. Most noticeable are oscillations of the unactuated ribs in the in-cone direction that die out very slowly. The experimental transients are also larger. The experimental rib torques saturated for the first two seconds but this might not explain the discrepancy between the experimental and simulated torques. It is more likely that the plant dynamics are not well modeled by the nominal coprime factorization. Moreover, the nonlinearities seem to play a more significant role in this noncollocated configuration because some of the ribs do not have local feedback to reduce their effects.

The experimental response with \mathbf{K}_{p2d} and a torque disturbance $D(13.5 \text{ Nm}, 2s, y)$ was marginally stable: One of the ribs unactuated along the in-cone direction entered a small limit cycle involving only its out-of-cone thruster and in-cone motion. The simulated response was comparable to the one shown in Figs. 15 and 16. It is believed that thruster deadband, coupling spring nonlinearities and thruster misalignment caused the occurrence of the limit cycle. A closed-

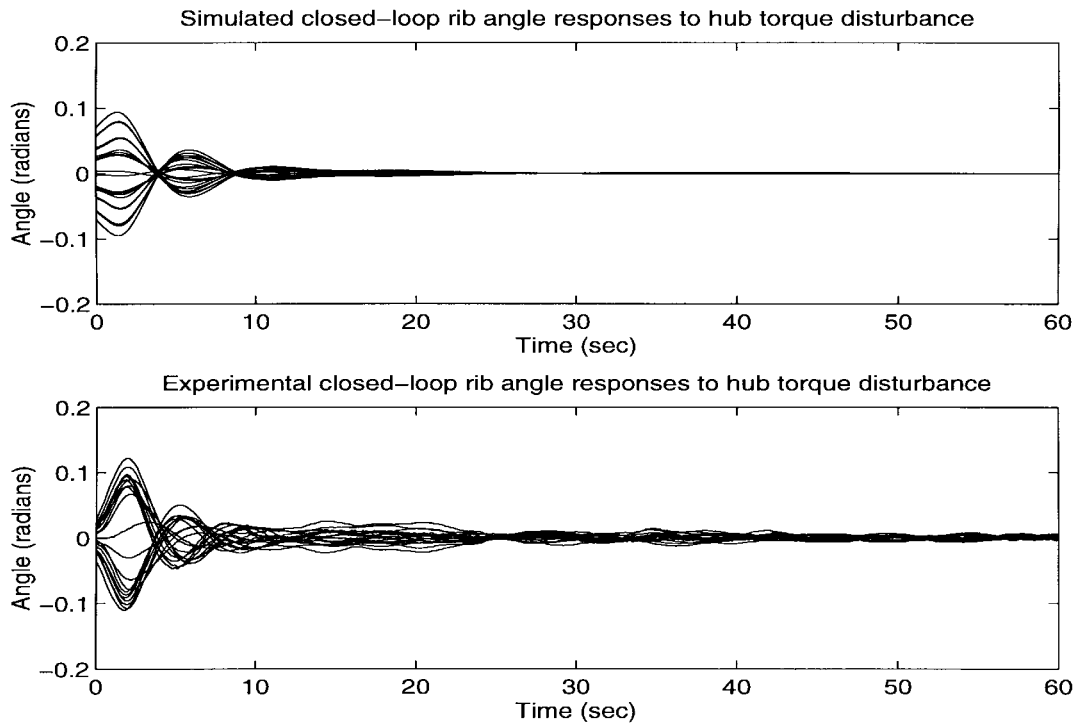


Fig. 13. Simulated and experimental closed-loop rib angle responses with K_{p1d} , $D(13.5 \text{ Nm}, 2s, y)$.

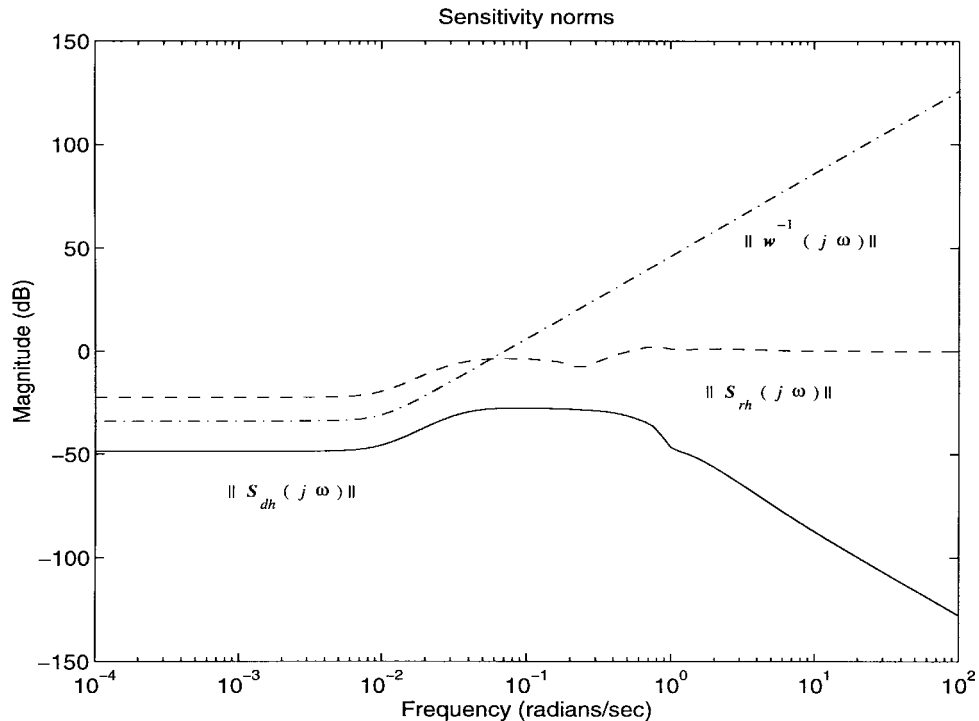


Fig. 14. Norms of $S_{dh}(j\omega)$ and $S_{rh}(j\omega)$ with K_2 .

loop experiment with a z -axis disturbance $D(6.8 \text{ Nm}, 2s, z)$ showed that K_{p2d} unequivocally destabilized Daisy even though the simulated nominal response was stable. Those input-dependent stability results hint at what could be significant nonlinear effects for this noncollocated configuration. The linear simulations showed very good nominal performance

while the design itself indicated robustness to reasonably large deviations in the modal parameters.

V. CONCLUSION

A new approach introduced in [3] to the robust control of LFSS using a coprime factor description of the plant's

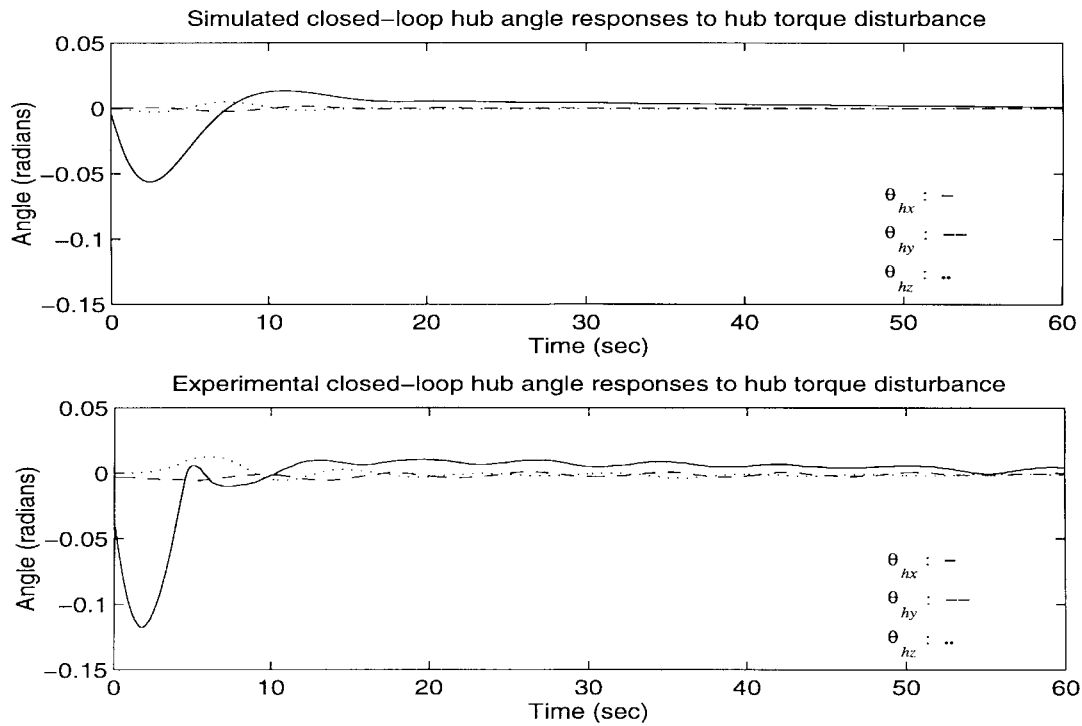


Fig. 15. Simulated and experimental closed-loop hub angle responses with K_{p2d} , $D(13.5 \text{ Nm}, 2s, x)$.

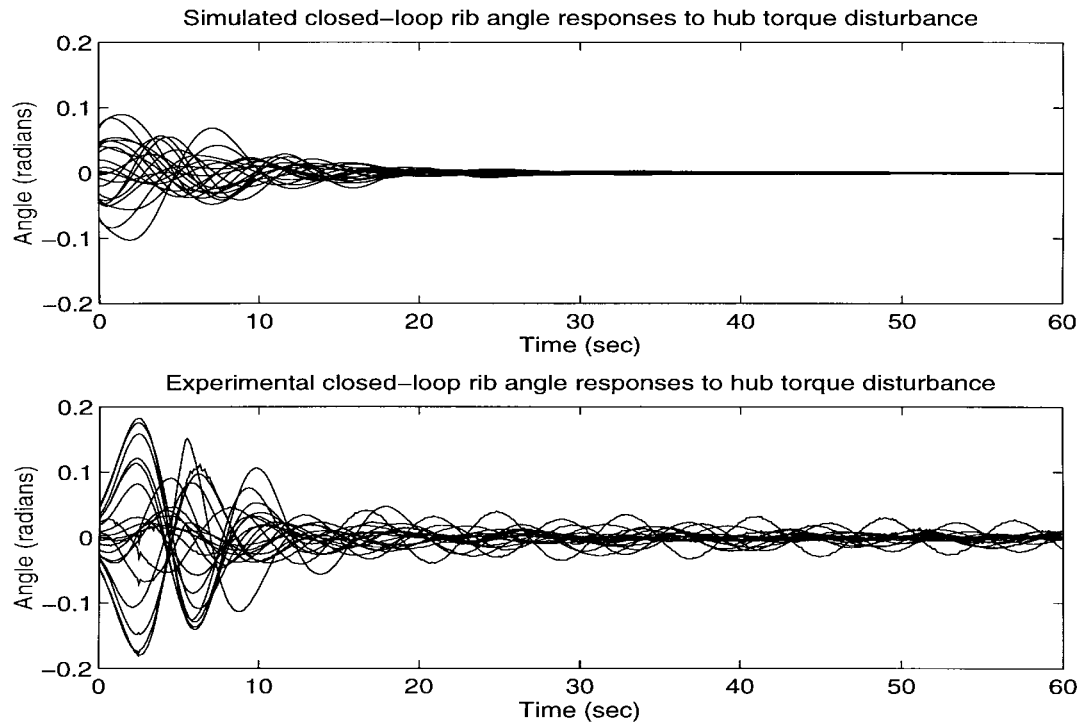


Fig. 16. Simulated and experimental closed-loop rib angle responses with K_{p2d} , $D(13.5 \text{ Nm}, 2s, x)$.

dynamics was presented. To illustrate the technique, two \mathcal{H}_∞ controllers were designed for collocated and noncollocated models of Daisy. These models have significant parameter uncertainty, yet the controllers designed using the coprime factorization technique were quite robust in simulations and achieved good performance levels in terms of rejection of hub

torque disturbances. Extensive experimentation has shown that a digital implementation of the collocated \mathcal{H}_∞ controller performed very well without the need of any experimental tuning. Digital implementation of the \mathcal{H}_∞ noncollocated controller was less successful at stabilizing Daisy even though the linear simulations showed good performance and robustness levels. It

was pointed out that nonlinearities such as thruster deadband seem to have played a major role in making Daisy much harder to stabilize in its noncollocated configurations. Further work is under way to include nonlinearities and sampling issues into the design technique.

APPENDIX

Proof of Proposition 1: An upper bound on $\|\Delta_{rp0}(j\omega)\|$ at each $\omega \in [0, \infty]$ is given by

$$\|\Delta_{rp0}(j\omega)\| \leq \sqrt{2} \max \{ \|\Delta_{N_{rp0}}(j\omega)\|, \|\Delta_{M_{rp0}}(j\omega)\| \}.$$

But

$$\begin{aligned} \|\Delta_{N_{rp0}}(j\omega)\| &= \left\| \frac{\frac{kd_{\max}}{c_{\max}} \Delta B_{sc}}{\left(j\omega + \frac{d_{\max}}{c_{\max}}\right)(j\omega + k)} \right\| \\ &\leq \left\| \frac{\frac{kd_{\max}}{c_{\max}}}{\left(j\omega + \frac{d_{\max}}{c_{\max}}\right)(j\omega + k)} \right\| \end{aligned}$$

and similarly

$$\begin{aligned} \|\Delta_{M_{rp0}}(j\omega)\| &\leq \left\| \frac{\frac{kd_{\max}}{c_{\max}}}{\left(j\omega + \frac{d_{\max}}{c_{\max}}\right)(j\omega + k)} \text{diag} \left\{ 0, 0, 0, \right. \right. \\ &\quad \left. \left. \frac{c_4 j\omega + d_4}{d_{\max}}, \dots, \frac{c_n j\omega + d_n}{d_{\max}} \right\} \right\| \\ &\leq \left\| \frac{\frac{kd_{\max}}{c_{\max}}}{\left(j\omega + \frac{d_{\max}}{c_{\max}}\right)(j\omega + k)} \right\| \\ &\quad \cdot \max_{i=4, \dots, n} \frac{|c_i j\omega + d_i|}{d_{\max}} \\ &\leq \left\| \frac{\frac{kd_{\max}}{c_{\max}}}{\left(j\omega + \frac{d_{\max}}{c_{\max}}\right)(j\omega + k)} \right\| \\ &\quad \cdot \left| \frac{c_{\max}}{d_{\max}} j\omega + 1 \right|. \end{aligned}$$

Hence

$$\begin{aligned} \|\Delta_{rp0}(j\omega)\| &\leq \frac{\sqrt{2}kd_{\max}}{c_{\max}} \frac{1}{\left|j\omega + \frac{d_{\max}}{c_{\max}}\right| \cdot |j\omega + k|} \\ &\quad \cdot \max \left\{ 1, \left| \frac{c_{\max}}{d_{\max}} j\omega + 1 \right| \right\} \\ &= \frac{\sqrt{2}kd_{\max}}{c_{\max}} \frac{1}{\left|j\omega + \frac{d_{\max}}{c_{\max}}\right| \cdot |j\omega + k|} \left| \frac{c_{\max}}{d_{\max}} j\omega + 1 \right| \end{aligned}$$

$$= \frac{\sqrt{2}}{\left| \frac{j\omega}{k} + 1 \right|} < |\mathbf{r}(j\omega)|.$$

Since \mathbf{r} is a unit, it follows that $\|\mathbf{r}^{-1}\Delta_{rp0}\|_{\infty} < 1$. ■

Proof of Proposition 2: The proof uses the submultiplicativity property of the norm $\|\cdot\|$. Assume \mathbf{K} is stabilizing and achieves (20), which implies that $\|w \mapsto z_1\|_{\infty} \leq 1$. This inequality says that the closed-loop system is robustly stable to all perturbations $\tilde{\Delta}_0 \in \mathcal{BRH}_{\infty}^{m \times (m+n)}$. Furthermore, (20) implies that $\|\mathbf{W}_q \mathbf{S}_r C_1 J_1 \tilde{\mathbf{M}}_0^{-1}\|_{\infty} \leq 1$. Then $\forall \omega \in \mathbb{R}$

$$\begin{aligned} q|w(j\omega)| \|(\mathbf{S}_{rh} C_1 J_1 \tilde{\mathbf{M}}_0^{-1})(j\omega)\| &\leq 1 \\ \implies \|\mathbf{S}_{rh}(j\omega)\| &\leq q^{-1} |w^{-1}(j\omega)| \|\tilde{\mathbf{M}}_0(j\omega) J_1^{-1} C_1^{\dagger}\| \\ \implies \|\mathbf{S}_{rh}(j\omega)\| &\leq q^{-1} |w^{-1}(j\omega)| \|\tilde{\mathbf{M}}_0 J_1^{-1} C_1^{\dagger}\|_{\infty}. \end{aligned}$$

But $q \geq \|\tilde{\mathbf{M}}_0 J_1^{-1} C_1^{\dagger}\|_{\infty}$, hence $\|\mathbf{S}_{rh}(j\omega)\| \leq |w^{-1}(j\omega)|$.

Now $\mathbf{S}_{dh} = (\gamma/d_{\max}) \mathbf{S}_{rh} C_1 J_1 \tilde{\mathbf{M}}_0^{-1} \tilde{\mathbf{N}}_0 J_2$, so our assumption implies that $\forall \omega$

$$\begin{aligned} \|\mathbf{S}_{dh}(j\omega)\| &= \frac{\gamma}{d_{\max}} \|(\mathbf{S}_{rh} C_1 J_1 \tilde{\mathbf{M}}_0^{-1} \tilde{\mathbf{N}}_0 J_2)(j\omega)\| \\ &\leq \frac{\gamma}{d_{\max}} \|(\mathbf{S}_{rh} C_1 J_1 \tilde{\mathbf{M}}_0^{-1})(j\omega)\| \|\tilde{\mathbf{N}}_0(j\omega) J_2\| \\ &\leq \frac{\gamma}{d_{\max}} q^{-1} |w^{-1}(j\omega)| \|\tilde{\mathbf{N}}_0(j\omega) J_2\| \\ &\leq q^{-1} d_{\max}^{-1} |w^{-1}(j\omega)| \|J_1^{-1} B_1\|. \end{aligned}$$

But $q \geq d_{\max}^{-1} \|J_1^{-1} B_1\|$, and therefore $\|\mathbf{S}_{dh}(j\omega)\| \leq |w^{-1}(j\omega)|$. ■

ACKNOWLEDGMENT

The authors wish to acknowledge the help and support provided by V. Pugliese, system manager, and R. S. K. Lee, graduate student, both from UTIAS, to carry out the experiments on Daisy. Lee also provided the drawing of Daisy in Fig. 6.

REFERENCES

- [1] G. J. Balas and J. C. Doyle, "Robustness and performance tradeoffs in control design for flexible structures," in *Proc. 1991 Amer. Contr. Conf.*
- [2] G. J. Balas, J. C. Doyle, K. Glover, A. Packard, and R. Smith, *μ -Analysis and Synthesis Toolbox: User's Guide*, The Mathworks Inc., 1991.
- [3] B. Boulet, B. A. Francis, P. C. Hughes, and T. Hong, "Robust control of large flexible space structures using a coprime factor plant description," in *Proc. 1994 Amer. Contr. Conf.*, Baltimore, MD.
- [4] ———, "Robust \mathcal{H}_{∞} control of large flexible space structures using a coprime factor plant description," Univ. Toronto, Dept. Elect. Comput. Eng., Syst. Contr. Group Rep. no. 9401, 1994.
- [5] S. A. Buddie, T. T. Georgiou, U. Özgüner, and M. C. Smith, "Flexible structure experiment at JPL and WPAFB: \mathcal{H}_{∞} controller designs," *Int. J. Contr.*, vol. 58, no. 1, pp. 1–19, 1993.
- [6] G. W. Crocker, P. C. Hughes, and T. Hong, "Real-time computer control of a flexible spacecraft emulator," *IEEE Contr. Syst. Mag.*, vol. 10, no. 1, pp. 3–8, Jan. 1990.
- [7] E. J. Davison, W. Gesing, and S. H. Wang, "An algorithm for obtaining the minimal realization of a linear time-invariant system and determining if a system is stabilizable-detectable," *IEEE Trans. Automat. Contr.*, vol. 23, pp. 1048–1054, Dec. 1978.
- [8] J. C. Doyle, K. Glover, P. P. Khargonekar, and B. A. Francis, "State-space solutions to standard \mathcal{H}_2 and \mathcal{H}_{∞} control problems," *IEEE Trans. Automat. Contr.*, vol. 34, pp. 831–847, Aug. 1989.
- [9] M. K. H. Fan, A. L. Tits, and J. C. Doyle, "Robustness in the presence of mixed parametric uncertainty and unmodeled dynamics," *IEEE Trans. Automat. Contr.*, vol. 36, pp. 25–38, Jan. 1991.

- [10] R. A. Horn and C. R. Johnson, *Matrix Analysis*. Cambridge, U.K.: Cambridge Univ. Press, 1990.
- [11] J. P. How, S. R. Hall, and W. M. Haddad, "Robust controllers for the middeck active control experiment using Popov controller synthesis," *IEEE Trans. Contr. Syst. Technol.*, vol. 2, no. 2, pp. 73–87, June 1994.
- [12] D. G. Laurin, "Development of an optical imaging system for shape monitoring of large flexible structures," Ph.D. dissertation, Univ. Toronto, Dept. Aerospace Eng., 1992.
- [13] K. B. Lim, P. G. Maghami, and S. M. Joshi, "Comparison of controller designs for an experimental flexible structure," *IEEE Contr. Syst. Mag.*, vol. 12, no. 3, pp. 108–118, June 1992.
- [14] D. C. McFarlane and K. Glover, *Robust Controller Design Using Normalized Coprime Factor Plant Descriptions*. New York: Springer-Verlag, 1990.
- [15] D. G. Meyer, "A fractional approach to model reduction," in *Proc. Amer. Contr. Conf.*, Atlanta, GA, 1988, pp. 1041–1047.
- [16] R. E. Skelton and P. C. Hughes, "Modal cost analysis for linear matrix-second-order systems," *ASME J. Dynamic Syst., Measurement, Contr.*, vol. 102, pp. 151–158, Sept. 1980.
- [17] R. S. Smith, C.-C. Chu, and J. L. Fanson, "The design of \mathcal{H}_∞ controllers for an experimental noncollocated flexible structure problem," *IEEE Trans. Contr. Syst. Technol.*, vol. 2, pp. 101–109, June 1994.
- [18] M. Vidyasagar, *Control System Synthesis: A Coprime Factorization Approach*. Cambridge, MA: MIT Press, 1985.



Benoit Boulet (S'88–M'92) was born in Saint-Tite, Québec, Canada, in 1967. He received the B.A.Sc. degree from Université Laval, Québec, in 1990, the M.Eng. degree from McGill University, Montréal, Canada, in 1992, and the Ph.D. degree from the University of Toronto, Canada, in 1996, all in electrical engineering.

He works for Hatch Associates, Ltd. as a consulting engineer in the area of metallurgical process control. He currently holds a Postdoctoral Industrial Research Fellowship from NSERC to work on ro-

bust fuzzy logic control of smelting furnaces at Hatch. His interests include \mathcal{H}_∞ control theory, robust control of large flexible structure, model validation for robust control, digital filter design based on Nevanlinna–Pick interpolation theory, real-time digital control systems, and fuzzy logic control.

Dr. Boulet was the recipient of an NSERC postgraduate scholarship, an FCAR scholarship, a University of Toronto Open Fellowship, and a W. C. Sumner Fellowship during his graduate studies.



Bruce A. Francis (S'73–M'75–SM'85–F'88) was born in Toronto, Canada. He received the B.A.Sc. and M.Eng. degrees in mechanical engineering and the Ph.D. degree in electrical engineering from the University of Toronto, Canada, in 1969, 1970, and 1975, respectively.

He has held research and teaching positions at the University of California at Berkeley, the University of Cambridge, Concordia University, McGill University, Yale University, the University of Waterloo, Caltech, and the University of Minnesota. He is presently a Professor of Electrical and Computer Engineering at the University of Toronto. He has coauthored three books, including *Optimal Sampled-Data Control Systems* (London: Springer-Verlag, 1995). His current research is in digital control and signal processing.

Dr. Francis was a corecipient of two Outstanding Paper Awards for papers appearing in the IEEE TRANSACTIONS ON AUTOMATIC CONTROL, and a corecipient of the 1991 IEEE W. R. G. Baker Prize Award.



Peter C. Hughes was born in 1940. He received the M.B.A. degree from York University, Toronto, Canada, in 1996.

He is a Professor at the University of Toronto and is founding Chairman of Dynacon, Inc. He is the author of *Spacecraft Attitude Dynamics* (New York: Wiley, 1986) and about 100 other refereed technical papers. He has held several visiting positions in government and business. His current main research interest is technology transfer.



Tony Hong was born in Sudbury, Ontario, Canada, in 1965. He received the B.A.Sc. and M.A.Sc. degrees in aerospace engineering from the University of Toronto, Canada, in 1987 and 1990, respectively. He is currently pursuing the Ph.D. degree in the field of spacecraft dynamics and control at the University of Toronto.

He is a Research Engineer for Dynacon Enterprises, Ltd., Toronto, Canada.